GDCh Research Article Angewandte International Edition Chemie www.angewandte.org

How to cite: *Angew. Chem. Int. Ed.* **2025**, e22386
doi.org/10.1002/anie.202522386

Gas Separation

Inverse CO_2-C_2H_2 Separation on the Low-Silica CHA Zeolite Through Cooperative Cation and Gas Molecule Migration Mechanism

Xiaohe Wang[+], Da Zheng[+], Jiatong Guo, Xiaona Liu, Nana Yan, Guohui Li,* Peng Guo, and Zhongmin Liu*

Abstract: Inverse CO_2/C_2H_2 separation is promising for direct C_2H_2 purification; however, designing cost-effective and CO_2-selective stable porous materials remains challenging. Herein, by precise Si/Al ratio design and inorganic cation regulation in low-silica CHA zeolites, we achieve excellent inverse CO_2/C_2H_2 separation based on the trapdoor effect via a cooperative cation and gas molecule migration mechanism, distinct from the transient and reversible cation deviation previously reported. The designed K-CHA exhibits high CO_2 capacity (3.51 mmol g^{-1}) and much lower C_2H_2 uptake (0.62 mmol g^{-1}) at 298 K and 1 bar, achieving an ideal adsorbed solution theory (IAST) selectivity of 4350, outperforming most metal-organic frameworks (MOFs) and zeolites. Breakthrough experiments confirmed the exceptional one-step C_2H_2 purification ability of K-CHA, yielding a productivity of 662.9 mmol kg^{-1}. Rietveld refinement located cation positions within CHA. Density functional theory (DFT) calculations and ab initio molecular dynamics simulations (AIMD) elucidated the separation mechanism that CO_2 interacts more strongly with K-CHA compared to C_2H_2, and the diffusion barrier for CO_2 passing through K^+-gated 8-rings is lower than C_2H_2. AIMD further revealed distinct trajectories and synergistic migration of the door-keeping K^+ ions and CO_2/C_2H_2 molecules during diffusion. This work provides new insights into the trapdoor mechanism, advancing our fundamental understanding.

Introduction

Acetylene (C_2H_2), a key precursor in chemical synthesis, is widely applied in the petrochemical industry, machinery manufacturing, and other advanced fields.[1–3] C_2H_2 can be produced through methane partial combustion or separated from steam cracking products of hydrocarbons, with CO_2 invariably co-produced as a major impurity.[4–6] Therefore, CO_2/C_2H_2 separation is an inevitable step to obtain high-purity C_2H_2.[3,4,6,7] However, due to the similar physicochemical properties of C_2H_2 and CO_2, including kinetic diameter, molecular dimensions, boiling point, dipole moment, and polarizability (Figure S1),[8–10] their separation process remains a significant challenge. Currently, CO_2/C_2H_2 separation primarily relies on solvent extraction and cryogenic distillation methods, both of which are energy- and cost-intensive.[1,2] In comparison, adsorptive separation based on porous solid materials, such as zeolites, carbon molecular sieves, metal-organic frameworks (MOFs), hydrogen-bonded organic frameworks (HOFs), and covalent-organic frameworks (COFs), etc., offers a promising alternative to conventional methods owing to superior energy efficiency.[11,12] For CO_2/C_2H_2 adsorptive separation, the porous solid materials can be designed as either C_2H_2-selective or CO_2-selective adsorbents depending on the different binding preference.[1,2,10] However, most of the aforementioned materials exhibit C_2H_2-selective adsorption since C_2H_2 has an electron-rich triple bond (C ≡ C) and acidic H atoms.[4,5,13–16] Therefore, high-purity C_2H_2 is typically obtained during the energy-intensive and less efficient desorption stage. In contrast, using CO_2-selective sorbents with inverse CO_2/C_2H_2 separation performance enables one-step production of high-purity C_2H_2 through an energy-efficient process, reducing energy consumption by approximately 40% compared to C_2H_2-selective adsorbents.[2,17,18] Nevertheless, developing effective CO_2-selective adsorbents remains a formidable and rarely achieved challenge.

Until now, only a few of the porous materials, such as zeolites,[19–22] MOFs,[2,17,18,23–28] and HOFs[29] have achieved inverse CO_2/C_2H_2 separation through strategies of regulating the adsorption sites and pore environment, kinetic sieving, flexible behavior with gate opening effect, etc. Among them, zeolites have attracted significant attention due to their

[*] Dr. X. Wang[+], J. Guo, Dr. X. Liu, Dr. N. Yan, Prof. P. Guo, Prof. Z. Liu
National Engineering Research Center of Lower-Carbon Catalysis Technology, Dalian Institute of Chemical Physics, Chinese Academy of Sciences, Dalian, Liaoning 116023, China
E-mail: yannana@dicp.ac.cn

D. Zheng[+], J. Guo, Dr. X. Liu, Prof. P. Guo, Prof. Z. Liu
University of Chinese Academy of Sciences, Beijing 100049, China

D. Zheng[+], Prof. G. Li
State Key Laboratory of Chemical Reaction Dynamics, Dalian Institute of Chemical Physics, Chinese Academy of Sciences, Dalian, Liaoning 116023, China
E-mail: ghli@dicp.ac.cn

Prof. G. Li
Interdisciplinary Research Center for Biology and Chemistry, Liaoning Normal University, Dalian, Liaoning 116029, China

[+] Both authors contributed equally to this work.

Additional supporting information can be found online in the Supporting Information section

cost-effectiveness and remarkable thermal and hydrothermal stabilities.[30–34] Recently, a novel trapdoor (cation gating) effect has been reported in zeolite adsorptive separation, which can exclusively recognize specific molecules, such as CO_2 and CO, and contribute to excellent separation performance in CO_2/CH_4, CO_2/N_2, and CO/N_2.[35–39] In general, the trapdoor effect occurs when the 8-ring pore openings necessary for gas molecular diffusion are occupied by the effective door-keeping cations in small-pore zeolites. During gas diffusion, CO_2 molecules with large quadrupole moments interact strongly with the door-keeping cations, inducing their movements and enabling CO_2 diffusion.[20,39,40] Gases like CH_4 and N_2 do not interact sufficiently with the cations to drive cation movement away, thus exhibiting molecular exclusion for efficient gas separation.[39,40] Since there are dramatic differences in both quadrupole moments (CO_2: -13.4×10^{-40} C·m^2; C_2H_2: $+20.5 \times 10^{-40}$ C·m^2) and electrostatic potentials (CO_2: C +0.700e, O −0.350e; C_2H_2: C −0.266e, H +0.266e) between CO_2 and C_2H_2,[9] we expect to achieve an effective CO_2/C_2H_2 separation via the trapdoor effect on cationic small-pore zeolites.

Moreover, reported research employs density functional theory (DFT) and the nudged elastic band (NEB) methods to reveal the trapdoor mechanism by analyzing the energy levels of gas molecules passing through 8-ring windows.[35,39,41] These conventional approaches require predefined initial and final states to locate minimum-energy paths, inherently imposing structural assumptions and risking overlooking favorable pathways like gas molecule-cation cooperativity. Therefore, investigating the dynamic trajectories of gating cations and gas molecules during gas adsorption is of significant importance. Ab initio molecular dynamics (AIMD) simulations, a powerful computational approach that combines quantum mechanical calculations with classical molecular dynamics, enable accurate modeling of dynamic processes at the atomic scale and are widely used to study gas diffusion in zeolite catalysis.[42,43] This approach effectively circumvents the need for structural presumptions and will reveal the intrinsic trapdoor mechanism, particularly the migration of gating cations and gas molecules during the adsorption process.

In this article, we design a small-pore K-CHA zeolite with outstanding inverse CO_2/C_2H_2 separation performance based on the trapdoor effect involving cooperative migration between gas molecules and K^+ ions. Gas adsorption measurements demonstrate that K-CHA exhibits excellent CO_2 selectivity, with a superior ideal adsorbed solution theory (IAST) selectivity of 4350 for an equimolar CO_2/C_2H_2 (50/50, v/v) mixture at 298 K. A C_2H_2 productivity of 662.9 mmol kg^{-1} with high purity was obtained from CO_2/C_2H_2 (50/50, v/v) breakthrough separation. In addition, the location of cations was identified by Rietveld refinement against powder X-ray diffraction (PXRD) data. The underlying mechanism was revealed by DFT and AIMD simulations, demonstrating that K-CHA exhibits preferential affinity for CO_2 and the diffusion barrier for CO_2 passing through single 8-rings (*s8rs*) of K-CHA is lower than C_2H_2. Furthermore, the migration trajectories of the door-keeping K^+ ions and CO_2/C_2H_2 by AIMD simulation during CO_2 and C_2H_2 adsorption reveal that K^+ ions located at *s8r*s and single 6-rings (*s6r*s) will migrate and redistribute cooperatively with gas molecules during adsorption and display different migration trajectories for CO_2 and C_2H_2. This study provides insights for rationally designing high-efficiency adsorbents while significantly enhancing the fundamental understanding of cation migration of the dynamic trapdoor mechanism.

Results and Discussion

Rational Design and Preparation of CHA Zeolite for Inverse CO_2/C_2H_2 Separation

In order to design high-performance small-pore zeolite adsorbents with inverse CO_2/C_2H_2 selectivity, the adsorption capacity and selectivity of CO_2 are two key factors that should be considered. Given the variable concentration (3%–50%) of CO_2 impurity in crude C_2H_2,[13,17,18,44,45] it is essential for optimal small-pore zeolite adsorbents to exhibit exceptional CO_2 adsorption capacity. Besides, these zeolites should have specific recognition ability for CO_2, but effectively exclude C_2H_2 molecules, thus achieving high selectivity in inverse CO_2/C_2H_2 separation. The trapdoor effect provides a foundation for designing high-performance small-pore zeolite adsorbents with inverse CO_2/C_2H_2 selectivity. For optimal separation performance through the trapdoor effect, an effective approach is to ensure an adequate concentration of molecular-recognizing door-keeping cations at the pore entrance of the diffusion channel. In this regard, the Si/Al ratio emerges as a crucial parameter, since it directly determines the number of inorganic cations per unit cell, thereby controlling the population of door-keeping cations. The cation location represents another critical parameter, as different types of cations preferentially occupy distinct crystallographic sites, regulating pore accessibility and influencing adsorption behavior. In this study, we focus on small-pore CHA zeolites, aiming to engineer materials with outstanding inverse CO_2/C_2H_2 separation performance through precise control of the Si/Al ratio and inorganic cations.

From the structural point of view, the CHA topology consists of double 6-rings (*d6r*s) and *cha* cages, featuring a three-dimensional (3D) channel system through 8-ring pore openings. Each *cha* cage connects to six adjacent cages via 8-ring pore openings. It should be noted that each unit cell contains 36 T atoms and nine *s8r*s.[46] Based on the design concept of the trapdoor effect, to allow the passage of CO_2 while excluding other gases, all of the 8-ring pore openings are expected to be obstructed (Scheme 1). In this case, the theoretical maximum Si/Al ratio of CHA should be less than or equal to 3. Therefore, low silica CHA zeolites were synthesized from an initial gel with a molar composition of 4.0 SiO_2: 0.5 Al_2O_3: 0.092 Na_2O: 1.067 K_2O: 171 H_2O and crystallized at 423 K for 6 days.[47] The PXRD pattern and SEM image (Figures S2 and S3) confirm the well-crystallinity of the as-synthesized CHA zeolites. XRF elemental analysis reveals an Si/Al ratio of 1.9, and the unit cell composition can be deduced as $|Na_{0.56}K_{12.76}|[Si_{23.57}Al_{12.42}O_{72}]$. Then, in order to investigate the effect of cation type, the as-synthesized CHA

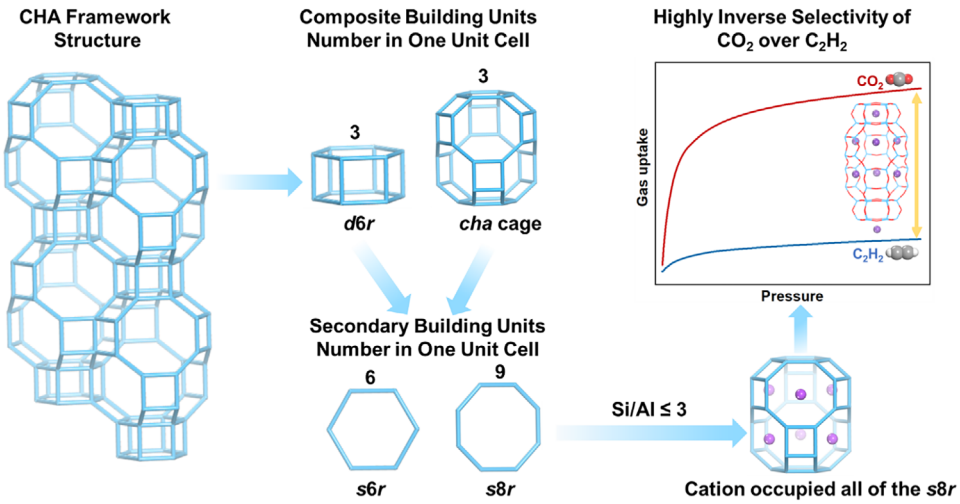

Scheme 1. The design principle of CHA zeolite for selective adsorption of CO_2 over C_2H_2.

zeolites were completely ion-exchanged with Na^+, K^+, and Cs^+, denoted as Na-CHA, K-CHA, and Cs-CHA, respectively (detailed in Supporting Information). The compositions of Na-CHA, K-CHA, and Cs-CHA were detailed in Table S1. The PXRD patterns and SEM images (Figures S2 and S3) show that Na-CHA, K-CHA, and Cs-CHA samples maintain their structural crystallinity after ion exchange. The porosity of ion-exchanged samples was characterized by N_2 sorption isotherms at 77 K (Figure S4), and the results indicated severely restricted pore accessibility in K-CHA and Cs-CHA samples.

CO_2/C_2H_2 Adsorption Separation Performance

The single component of CO_2 and C_2H_2 gas adsorption isotherms on Na-CHA, K-CHA, and Cs-CHA were collected at 298 K. Na-CHA demonstrates high adsorption capacities for both CO_2 (4.07mmo l g^{-1}) and C_2H_2 (3.92 mmol g^{-1}) at 298 K and 1 bar, as shown in Figure 1a,b. Compared to Na-CHA, Cs-CHA shows a dramatic decrease in C_2H_2 adsorption capacity (0.35 mmol g^{-1}), while simultaneously exhibiting decreased CO_2 adsorption (1.45 mmol g^{-1}). Notably, K-CHA not only exhibits a low C_2H_2 adsorption capacity of 0.62 mmol g^{-1}, but also maintains a relatively high CO_2 uptake of 3.51 mmol g^{-1}, which is comparable to that of the most state-of-the-art CO_2-selective materials, such as Sr/K-HEU (2.21 mmol g^{-1}),[20] $NaAlO_2$@MOR(0.5) (2.69 mmol g^{-1}),[22] ALF (3.85 mmol g^{-1}),[18] Zn-ox-mtz (3.07 mmol g^{-1}),[17] and HOF-FJU-88 (2.66 mmol g^{-1})[29] (Figure 1d and Table S2). Remarkably, K-CHA has superior CO_2 adsorption capacity in the low-pressure region, reaching 2.0 mmol g^{-1} at 298 K and 0.05 bar, which is apparently higher than that of reported zeolite materials such as Sr/K-HEU (1.56 mmol g^{-1}),[20] $NaAlO_2$@MOR(0.5) (1.57 mmol g^{-1}),[22] and Na-GIS (0.65 mmol g^{-1}),[19] and most of the MOF and HOF materials[2] (Figure 1c). Such an excellent gas adsorption capacity in the low-pressure region could endow K-CHA with a prominent capacity to capture trace amounts of CO_2, which is vital in industrial applications.

To evaluate the separation performance of Na-CHA, K-CHA, and Cs-CHA, the IAST was employed to evaluate the separation selectivity for an equimolar CO_2/C_2H_2 mixture (Figures S5–S8). As shown in Figure 1d, Na-CHA exhibits a low CO_2/C_2H_2 selectivity of 1.8 at 298 K and 1 bar owing to the high adsorption capacity of both CO_2 and C_2H_2. Although Cs-CHA exhibits relatively low C_2H_2 adsorption capacity, its simultaneously low CO_2 uptake results in a moderate CO_2/C_2H_2 selectivity of 8.1. Encouragingly, K-CHA achieves an ISTA selectivity of 4350 for CO_2/C_2H_2, which is greatly higher than that of most reported CO_2-selective materials such as HOF-FJU-88 (1894),[29] Zn-ox-mtz (1065),[17] and GIS-3.1 (2650)[19] (Figure 1d and Table S2). In addition, the coverage-dependent isosteric heat of adsorption (Q_{st}), which evaluates the affinity between adsorbed gas and the adsorbent, was calculated through virial fitting based on adsorption isotherms measured at 273 and 298 K (Figures S9 and S10). The Q_{st} of K-CHA for CO_2 is 14.8 kJ mol^{-1} at near-zero coverage (Figure S10). As CO_2 adsorption increases, the Q_{st} progressively rises to 33.8 kJ mol^{-1}. The moderate adsorption enthalpy for CO_2 indicates facile regeneration of K-CHA under mild conditions. Therefore, the superior CO_2 capture performance, high selectivity of CO_2/C_2H_2, and low CO_2 isosteric heat of adsorption make K-CHA a promising candidate for inverse CO_2/C_2H_2 separation.

To further evaluate the practical CO_2/C_2H_2 separation properties of K-CHA, breakthrough experiments for an equimolar CO_2/C_2H_2 (50/50, v/v) mixture were performed on the activated zeolites with a flow rate of 2 mL min^{-1} at 298 K and 1 bar (Figure 1e). As we expected, direct one-step purification of C_2H_2 was successfully achieved on K-CHA with a separation factor of 6.54. C_2H_2 quickly reached adsorption saturation and was eluted from the packed column immediately, with a retention time of 0.82 min g^{-1}. CO_2 was trapped in the packed column for 15.67 min g^{-1} with a dynamic adsorption capacity of 2.55 mmol g^{-1}. The breakthrough interval time between C_2H_2 and CO_2 was

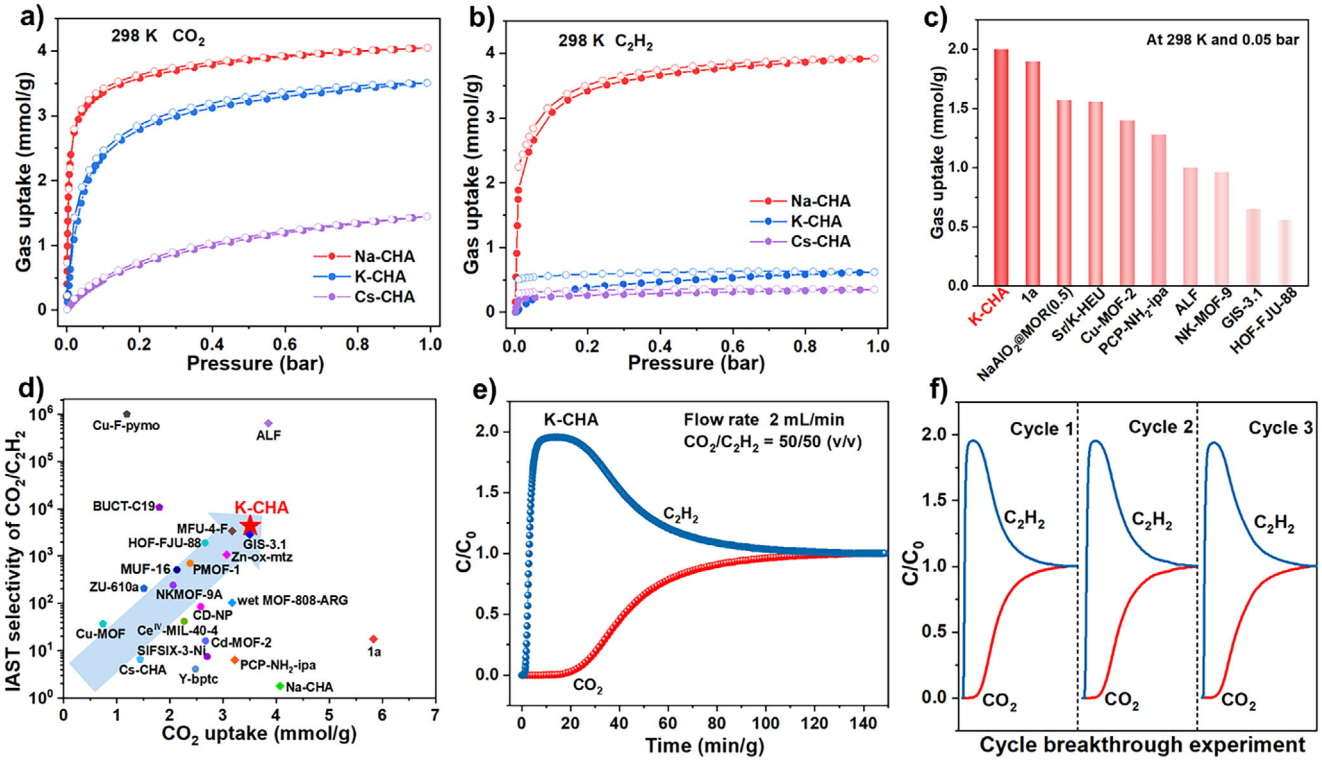

Figure 1. The single-component adsorption (solid circle) and desorption (hollow circle) isotherms of CO_2 and C_2H_2 for Na-CHA, K-CHA, and Cs-CHA at 298 K: a) CO_2 adsorption/desorption isotherms, b) C_2H_2 adsorption/desorption isotherms. c) Comparison of CO_2 uptake at 298 K and 0.05 bar among different CO_2-selective materials. d) Comparison of IAST CO_2/C_2H_2 (50/50, v/v) selectivity and CO_2 uptake (mmol g^{-1}) of advanced CO_2-selective adsorbents at 298 K and 1 bar. e) The breakthrough experimental curves for the equimolar CO_2/C_2H_2 (50/50, v/v) mixture on K-CHA with a flow rate of 2 mL min^{-1} at 298 K and 1 bar. f) The cycle breakthrough experimental curves for the equimolar CO_2/C_2H_2 (50/50, v/v) mixture on K-CHA with a flow rate of 2 mL min^{-1} at 298 K and 1 bar.

approx. 15 min g^{-1}, yielding high-purity C_2H_2 (>99.6%) of 662.9 mmol kg^{-1} (Figure S13). Furthermore, multiple cycling breakthrough experiments under the same condition were carried out. K-CHA maintained excellent inverse CO_2/C_2H_2 separation performance while sustaining high-purity C_2H_2 production over three continuous cycles (Figure 1f and Table S3). Additionally, there were no obvious changes in the PXRD patterns of K-CHA after breakthrough experiments (Figure S14). It suggests that K-CHA has prominent stability and recyclability for the challenging inverse CO_2/C_2H_2 separation. It is worth noting that the majority of adsorbed CO_2 and C_2H_2 was rapidly released during argon purging at 298 K in the desorption process, and the remaining fraction could be completely desorbed when the temperature was raised to 373 K (Figure S15).

In addition, the adsorption behavior of K-CHA for other hydrocarbons, including CH_4, C_2H_4, and C_2H_6 was investigated. As shown by the adsorption isotherms in Figure S16, all of the tested hydrocarbons were excluded by K-CHA. A breakthrough experiment confirmed that complete separation of CO_2 and hydrocarbon mixtures can be achieved with K-CHA (Figure S17). All of the hydrocarbons were rapidly eluted from the packed column, and CO_2 was trapped. Therefore, K-CHA is a promising material for efficiently capturing CO_2 from CO_2-containing hydrocarbon mixtures, especially for C_2H_2 purification.

Effect of Cation Type and Location on Adsorption Properties

Inorganic cation type significantly affects the CO_2/C_2H_2 separation performance of CHA. To locate the positions of Na^+, K^+, and Cs^+ ions and elucidate these cation effects, Rietveld refinement against high-resolution PXRD data was conducted on dehydrated Na-CHA, K-CHA, and Cs-CHA. Na^+, K^+, and Cs^+ ions occupy distinct locations within the CHA framework due to their different ionic radii and coordination ability with adjacent framework oxygen atoms, as shown in Figures 2, S18, and S19. Na^+ ions with smaller ionic radii occupy two crystallographically distinct sites in Na-CHA, located at the center of *s6r*s and the off-center of *s8r*s (Figure S18). There are 5.28 Na^+ ions located at *s6r*s per unit cell with a closest Na–O distance of 2.49 Å, and 7.38 Na^+ ions at *s8r*s with a closest Na–O distance of 2.45 Å (Table S5). Theoretically, 2 out of 9 *s8r*s per unit cell remain unoccupied by Na^+, leaving these *s8r* windows accessible for gas diffusion, which is consistent with the detectable but limited N_2 uptake at 77 K in Figure S4. Furthermore, the relatively smaller Na^+ ions exhibit weaker interactions with the local environment of 8-rings, making them less effective in distinguishing between CO_2 and C_2H_2.[39,40,48] Therefore, Na-CHA exhibits simultaneous high adsorption capacities for both CO_2 and C_2H_2.

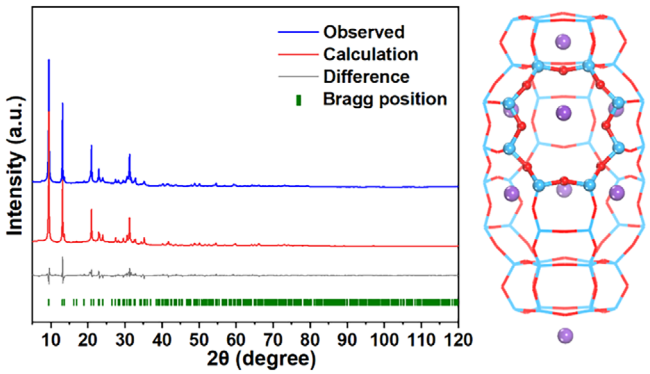

Figure 2. The final Rietveld refinement plots and crystallographic structure of K-CHA. The observed, calculated, and difference curves are in blue, red, and black, respectively. The vertical bars (green line) indicate the positions of the Bragg peaks (λ = 1.5406 Å). The Si, O, and K atoms are shown in blue, red, and purple, respectively.

In Cs-CHA, the larger Cs^+ ions preferentially concentrate at the center of *s8r*s with the closest Cs–O distance of 3.18 Å (Figure S19). All the openings of *s8r*s were occupied by Cs^+ ions. The larger Cs^+ ions exhibit stronger interactions with the *s8r*s local environment, leading to a high energy barrier for the movement of Cs^+ in the trapdoor process.[39] Additionally, the interaction between CO_2 and the extra-framework cation decreases as the cation radius increases.[48] Consequently, moving Cs^+ away from the *s8r* is more challenging than Na^+ and K^+. As a result, Cs-CHA exhibits the lowest capacities for both CO_2 and C_2H_2.

Rietveld refinement of K-CHA revealed that K^+ ions with a medium ion radius preferentially occupy the off-center of *s8r* with the closest K–O distance of 2.81 Å (Figure 2 and Table S5). The remaining minority of K^+ ions is located at the center of *d6r*s and the center above the plane of *s6r*s. The population of K^+ ions at *s8r*s, *d6r*s, and *s6r*s per unit cell are 9, 1.89, and 1.44, respectively (Table S5). All of the 8-ring pore openings are occupied by K^+ ions, which effectively function as door-keeping cations for the molecular recognition. CO_2 molecules can interact strongly with K^+ ions, providing sufficient energy to move the door-keeping K^+ ions away from the *s8r* windows, and thus gain access to the *cha* cage. Whereas, for C_2H_2, the weaker interaction of C_2H_2 molecules with K^+ ions and the electrostatic repulsion between K^+ ions and the positive center of C_2H_2 (H atoms) make it difficult to induce K^+ ions away from the *s8r* windows.[9,20] Thus, K-CHA has excellent inverse CO_2/C_2H_2 separation performance.

The Mechanism of CO_2/C_2H_2 Separation on K-CHA Revealed by GCMC/MD, DFT, and AIMD Simulations

Although it's established that the trapdoor effect makes K-CHA efficient for CO_2/C_2H_2 separations, the underlying mechanisms remain elusive. Two critical challenges remain unresolved: i) the precise molecular-level interactions between K-CHA and C_2H_2/CO_2, and ii) the dynamic migration behavior of K^+ ions during gas diffusion. To

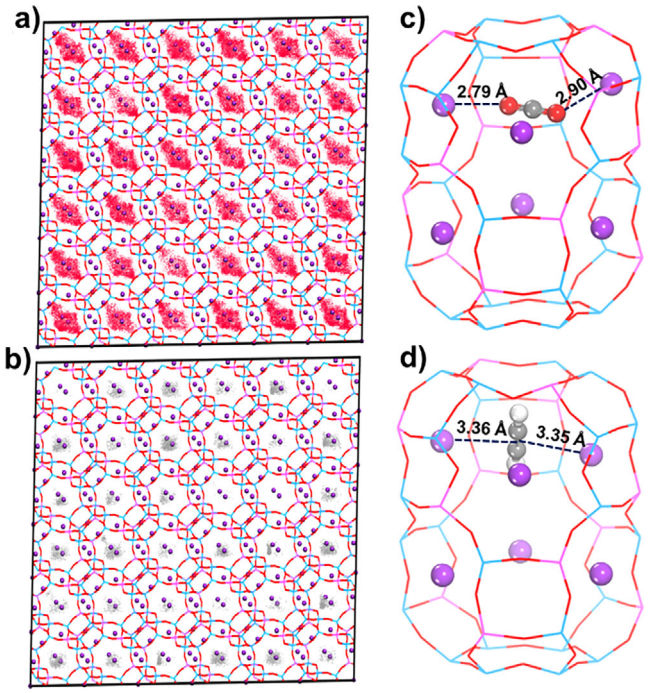

Figure 3. The probability density distributions and the optical binding sites of CO_2 a), c) and C_2H_2 b), d) within K-CHA at 298 K determined from GCMC/MD and DFT simulations. The Si, O, Al, K, C, and H atoms are shown in blue, red, pink, purple, gray, and white, respectively.

elucidate these questions, we conducted a series of computational simulations. First, the hybrid grand canonical Monte Carlo/molecular dynamics (GCMC/MD) and DFT simulations were carried out to investigate the host–guest interactions between the K-CHA framework and CO_2/C_2H_2. Since Al distribution in the K-CHA framework significantly influences the stability and migration ability of K^+ ions at different sites (*s8r*, *s6r*, and *d6r*), a series of possible structural models were optimized to obtain the stable structure prior to the simulations, and then the most stable structure was selected as the basis for subsequent GCMC/MD and DFT simulations (Figure S20).

To ensure a fair comparison in the GCMC/MD simulations, a supercell (6 x 6 x 6) containing 1728 Si atoms, 864 Al atoms, 5184 O atoms, and 864 K^+ ions was built. As outlined in Figures 3 and S21, all of the CO_2 and C_2H_2 gas molecules are located in the *cha* cage, and the density distribution of CO_2 is obviously higher than that of C_2H_2, indicating the higher adsorption capacity and stronger adsorption strength of CO_2 than that of C_2H_2, consistent with the practical separation experiments. In addition, the probable orientations and binding configurations of CO_2 and C_2H_2 in K-CHA have been elucidated. CO_2 molecules interact strongly with K^+ ions, showing shorter K···O (CO_2) distances of 2.79 and 2.90 Å (Figure 3c). C_2H_2 displays weaker binding affinity, with longer K···C ≡ C (C_2H_2) distances of 3.35 and 3.36 Å (Figure 3d). The distinct host–guest interaction for CO_2 and C_2H_2 correlates well with the observed adsorption behaviors.

Additionally, AIMD simulations combined with the enhanced sampling method (detailed in Supporting

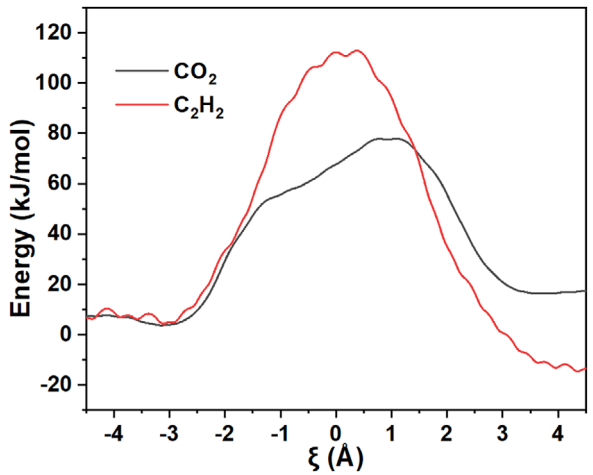

Figure 4. Free energy profiles of CO_2 and C_2H_2 passing through the 8-ring window that connects two neighboring *cha* cages. ξ defines the diffusion path of gas molecules from one cage ($\xi < 0$) through the *s8r* windows ($\xi = 0$) into the neighboring cage ($\xi > 0$).

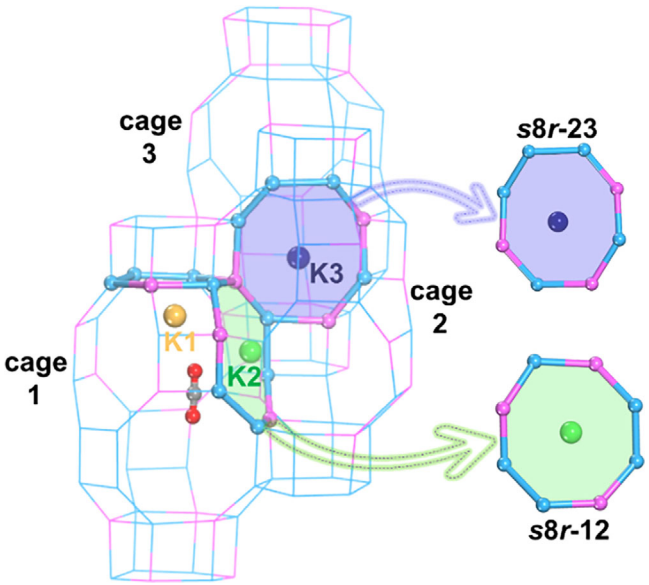

Figure 5. Structural description of three adjacent *cha* cages in K-CHA. The Si, O, Al, and C atoms are shown in blue, red, pink, and gray, respectively. The key K^+ ions (denoted as K1, K2, and K3) are highlighted in yellow, green, and navy. The framework O atoms were omitted for clarity.

Information) were further employed to investigate CO_2/C_2H_2 diffusion and K^+ ion migration. Since all the *s8r* windows are initially occupied by K^+ ions, CO_2 and C_2H_2 molecules must adjust their orientations to navigate through these narrow openings into adjacent *cha* cages and the K^+ ions must simultaneously move away from their initial position temporarily or even permanently in the diffusion process. Consequently, both the molecular reorientation and the migration of K^+ ions contribute to the diffusion energy barrier that must be overcome by the CO_2/C_2H_2 molecules. The free energy profiles of CO_2 and C_2H_2 diffusion through the *s8r* of K-CHA were constructed along a pre-defined collective variable (Figure S22), ξ, which uniquely defines the diffusion path of gas molecules from one cage ($\xi < 0$) through the *s8r* windows ($\xi = 0$) into the neighboring cage ($\xi > 0$). The difference in diffusion energy barriers also arises from the distinct physicochemical properties of CO_2/C_2H_2. As shown in Figure 4, the energy barrier of CO_2 is significantly lower than that of C_2H_2, which indicates that CO_2 molecules diffuse more easily than C_2H_2 in K-CHA. This result is in agreement with the GCMC/MD simulations (Figure 3c,d) and kinetic adsorption experiments (Figure S23). As depicted in Figure S23, CO_2 reaches adsorption saturation significantly faster than C_2H_2.

Further analysis of the CO_2/C_2H_2 diffusion trajectories shows that some K^+ ions relocate during CO_2/C_2H_2 diffusion process. For clarity of description, the key K^+ ions of interest are denoted as K1, K2, and K3 (Figure 5). Three adjacent *cha* cages are labeled as cage 1, 2, and 3. The *s8r* connecting cages 1 and 2 is designated as *s8r-12*, while that between cages 2 and 3 is termed *s8r-23*. Figure 6 presents the snapshots of adsorption configurations and trajectories in detail. When CO_2 diffuses across the *s8r* window (*s8r-12*) from cage 1 into cage 2, the K^+ ion (K2, green in Figure 6a) originally located at the *s8r*-12 first migrates to the cavity of cage 2, then falls into the adjacent *s8r*-23 as illustrated in Figure 6a. And the K3, which was originally located at the *s8r*-23 will move to the *s6r* of the neighboring cage 3. At the same time, the K1, which was initially located at the *s6r* in cage 1, will migrate to the vacant *s8r-12* site. The highest energy barrier for CO_2 diffusion throughout the process is 77.8 kJ mol^{-1}. These results demonstrate that CO_2 diffusion via the trapdoor effect in K-CHA involves cooperative migration between CO_2 molecules and K^+ ions. The K^+ ions at *s8rs* undergo hopping between different crystallographic sites during CO_2 adsorption, rather than a transient and reversible cation deviation, and K^+ ions at *s6rs* also participate in the whole process. To our knowledge, the phenomenon of cation migration and rearrangement between distinct crystallographic sites during adsorption has been observed on flexible zeolites, such as Cd^{2+} relocation in Cd-Rho during water adsorption and cation rearrangement of K-RHO and Na-MER during CO_2 adsorption.[36,49,50]

In addition, when C_2H_2 diffusion across the *s8r* as shown in Figure 6b, its orientation is different from CO_2, parallel to the *s8r* plane, and the highest energy barrier for C_2H_2 diffusion increases to 116.5 kJ mol^{-1}. The migration trajectories of K^+ ions also exhibit significant differences. When C_2H_2 passes through *s8r-12*, K2 first slides into the cavity of cage 2, and then locates at the *s6r* of cage 2. Meanwhile, K1 located at the *s6r* of cage 1 migrates to the vacant *s8r-12* window, exhibiting analogous migration behavior in CO_2. And there is no migration occurring on K3. AIMD simulations reveal distinct behaviors of CO_2/C_2H_2 diffusion and K^+ ions migration during CO_2/C_2H_2 adsorption on K-CHA, further elucidating the underlying reasons for the different adsorption performances. These findings offer new perspectives and solid foundations for understanding the trapdoor mechanism.

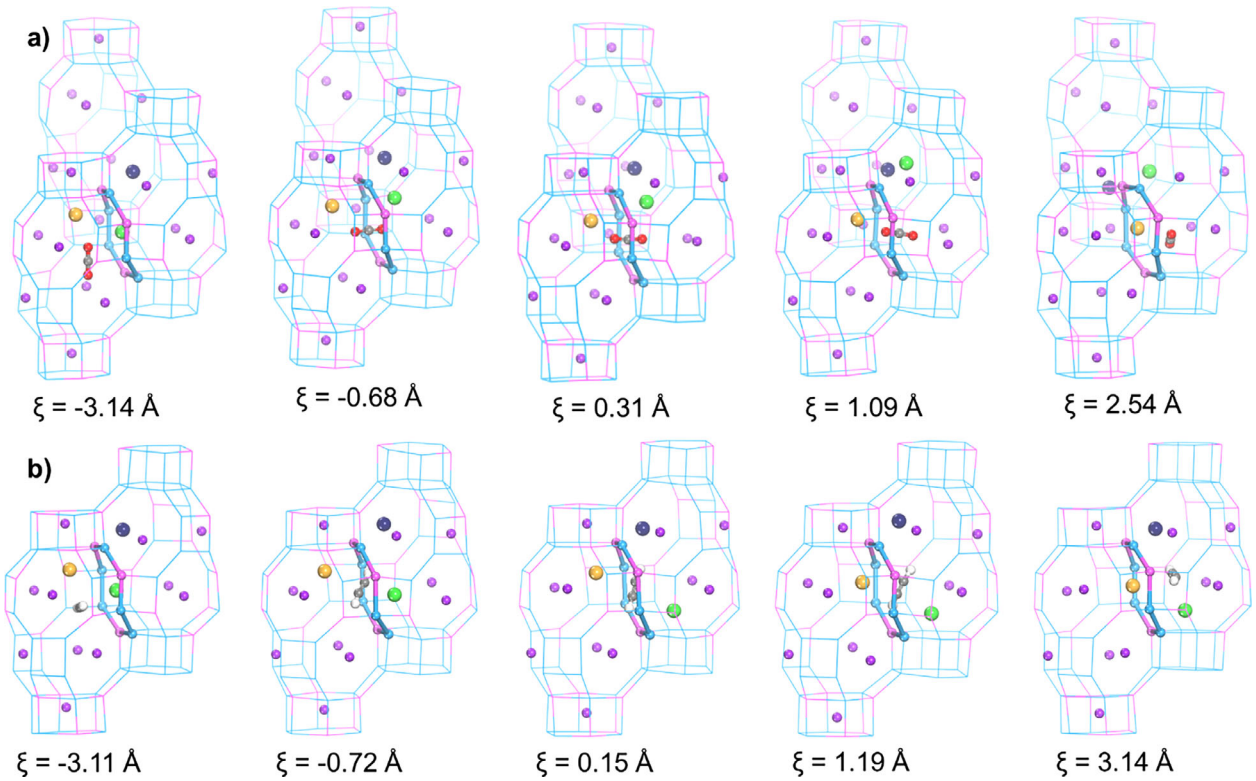

Figure 6. Snapshots of the selected trajectories of the structures of CO_2 a) and C_2H_2 b) diffusion in K-CHA by AIMD simulations. The Si, O, Al, K, C, and H atoms are shown in blue, red, pink, purple, gray, and white, respectively. The key K^+ ions (denoted as K1, K2, and K3 in Figure 5) are highlighted in yellow, green, and navy. The framework O atoms were omitted for clarity.

Conclusion

In summary, we propose a rational design strategy for developing zeolite-based adsorbents with preferential CO_2 adsorption based on precise manipulation of the trapdoor effect and apply AIMD simulations to the trapdoor process. Excellent inverse CO_2/C_2H_2 separation performance has been achieved on the designed low-silica K-CHA zeolites by implementing this strategy, and theoretical calculations further unveil a cooperative migration mechanism between door-keeping cations and gas molecules during the trapdoor process. Door-keeping K^+ ions permit the passage of CO_2 within the K-CHA framework while selectively excluding C_2H_2, as evidenced by static adsorption uptake at 298 K and 1 bar and calculated IAST selectivity of 4350. Breakthrough experiments further confirm the exceptional one-step purification ability of K-CHA for C_2H_2, with a dynamic selectivity of 6.54 and yielding a C_2H_2 productivity of 662.9 mmol kg^{-1}. Besides, all the *s8rs* connecting *cha* cages were occupied by K^+ ions, and the other K^+ ions located at the *d6rs* and *s6rs*, identified by Rietveld refinement. GCMC/MD, DFT, and AIMD simulations of the supercell K-CHA model further confirm its preferential affinity for CO_2, demonstrating a lower diffusion barrier for CO_2 passing through K^+-gated *s8rs* of K-CHA compared to C_2H_2. The interaction between the door-keeping K^+ ions and CO_2/C_2H_2 gas molecules was also revealed by AIMD simulations. Notably, the results demonstrate that cooperative migration occurs between K^+ ions and CO_2/C_2H_2 molecules during gas diffusion, where K^+ ions relocate to other crystallographic sites rather than undergoing transient reversible displacements from *s8rs*. The molecular orientations of CO_2/C_2H_2 diffusion through *s8rs* and the migration trajectories of K^+ ions exhibit fundamentally distinct behavior. Theoretical simulations uncover the underlying mechanism of the trapdoor effect. In conclusion, this work presents a strategy for designing zeolites with inverse CO_2/C_2H_2 separation performance based on the trapdoor effect and elucidates the mechanism, offering new perspectives for both material design and mechanism exploration.

Acknowledgements

This work is supported by the National Natural Science Foundation of China (No. 22288101, 22372156, and 22302195) and Liaoning Revitalization Talents Program (XLYC2203179).

Conflict of Interests

The authors declare no conflict of interest.

Data Availability Statement

The data that support the findings of this study are available in the Supporting information of this article. CCDC deposition

Numbers 2475185 (for Na-CHA), 2475174 (for K-CHA), and 2475176 (for Cs-CHA) contain the supplementary crystallographic data for this paper. These data are provided free of charge by the joint Cambridge Crystallographic Data Centre and Fachinformationszentrum Karlsruhe via www.ccdc.cam.ac.uk/structures/.

Keywords: AIMD simulations · Cation migration · Inverse CO_2/C_2H_2 separation · Low-silica CHA zeolite · Trapdoor mechanism

[1] X. Wang, H. Liu, Y. Li, X. Yang, F. Gao, X. Wang, Z. Kang, W. Fan, D. Sun, *Coord. Chem. Rev.* **2023**, *482*, 215093, https://doi.org/10.1016/j.ccr.2023.215093.

[2] Z. Zhang, D. Zhao, *Chem. Bio. Eng.* **2024**, *1*, 366–380, https://doi.org/10.1021/cbe.4c00035.

[3] J.-S. Zou, Z.-P. Wang, Y. H. Andaloussi, J. Xue, W. Zhang, B. E. G. Lucier, Z. Zhang, Y. Jia, X.-C. Wu, J. Li, Y. Huang, M. J. Zaworotko, G. Chen, S. Chen, Y.-L. Peng, *Nat. Commun.* **2025**, *16*, 2598, https://doi.org/10.1038/s41467-025-57972-7.

[4] R. Matsuda, R. Kitaura, S. Kitagawa, Y. Kubota, R. V. Belosludov, T. C. Kobayashi, H. Sakamoto, T. Chiba, M. Takata, Y. Kawazoe, Y. Mita, *Nature* **2005**, *436*, 238–241, https://doi.org/10.1038/nature03852.

[5] J.-P. Zhang, X.-M. Chen, *J. Am. Chem. Soc.* **2009**, *131*, 5516–5521, https://doi.org/10.1021/ja8089872.

[6] P. Pässler, W. Hefner, K. Buckl, H. Meinass, A. Meiswinkel, H.-J. Wernicke, G. Ebersberg, R. Müller, J. Bässler, H. Behringer, D. Mayer, in *Ullmann's Encyclopedia of Industrial Chemistry*, Wiley-VCH, Weinheim, Germany **2011**.

[7] H. Schobert, *Chem. Rev.* **2014**, *114*, 1743–1760, https://doi.org/10.1021/cr400276u.

[8] J.-R. Li, R. J. Kuppler, H.-C. Zhou, *Chem. Soc. Rev.* **2009**, *38*, 1477–1504, https://doi.org/10.1039/b802426j.

[9] R. Eguchi, S. Uchida, N. Mizuno, *Angew. Chem. Int. Ed.* **2012**, *51*, 1635–1639, https://doi.org/10.1002/anie.201107906.

[10] K.-J. Chen, H. S. Scott, D. G. Madden, T. Pham, A. Kumar, A. Bajpai, M. Lusi, K. A. Forrest, B. Space, J. J. Perry, M. J. Zaworotko, *Chem* **2016**, *1*, 753–765, https://doi.org/10.1016/j.chempr.2016.10.009.

[11] Y. X. Wang, S. B. Peh, D. Zhao, *Small* **2019**, *15*, 1900058.

[12] L. Yang, S. Qian, X. Wang, X. Cui, B. Chen, H. Xing, *Chem. Soc. Rev.* **2020**, *49*, 5359–5406, https://doi.org/10.1039/C9CS00756C.

[13] S. Liu, X. Han, Y. Chai, G. Wu, W. Li, J. Li, I. da Silva, P. Manuel, Y. Cheng, L. L. Daemen, A. J. Ramirez-Cuesta, W. Shi, N. Guan, S. Yang, L. Li, *Angew. Chem. Int. Ed.* **2021**, *60*, 6526–6532, https://doi.org/10.1002/anie.202014680.

[14] Y. Yang, H. Zhang, Z. Yuan, J.-Q. Wang, F. Xiang, L. Chen, F. Wei, S. Xiang, B. Chen, Z. Zhang, *Angew. Chem. Int. Ed.* **2022**, *61*, e202207579, https://doi.org/10.1002/anie.202207579.

[15] X. Wang, H. Liu, M. Sun, F. Gao, X. Feng, M. Xu, W. Fan, D. Sun, *Angew. Chem. Int. Ed.* **2025**, *64*, e202420801, https://doi.org/10.1002/anie.202420801.

[16] J. Zhang, H. Zheng, F. Chen, Z. Wang, H. Li, F. Sun, D. Zhao, V. Valtchev, S. Qiu, Q. Fang, *Angew. Chem. Int. Ed.* **2025**, *64*, e202500161, https://doi.org/10.1002/anie.202500161.

[17] S.-Q. Yang, R. Krishna, H. Chen, L. Li, L. Zhou, Y.-F. An, F.-Y. Zhang, Q. Zhang, Y.-H. Zhang, W. Li, T.-L. Hu, X.-H. Bu, *J. Am. Chem. Soc.* **2023**, *145*, 13901–13911, https://doi.org/10.1021/jacs.3c03265.

[18] Z. Zhang, Z. Deng, H. A. Evans, D. Mullangi, C. Kang, S. B. Peh, Y. Wang, C. M. Brown, J. Wang, P. Canepa, A. K. Cheetham, D. Zhao, *J. Am. Chem. Soc.* **2023**, *145*, 11643–11649, https://doi.org/10.1021/jacs.3c01705.

[19] G. Deng, K. Cheng, B. Meng, X. Shi, X. Liu, Y. Zhou, J. Wang, *Sep. Purif. Technol.* **2024**, *340*, 126764, https://doi.org/10.1016/j.seppur.2024.126764.

[20] J. Jia, N. Yan, X. Lian, S. Liu, B. Yue, Y. Chai, G. Wu, J. Xu, L. Li, *Angew. Chem. Int. Ed.* **2024**, *64*, e202419091, https://doi.org/10.1002/anie.202419091.

[21] Y. Ren, Y. Chen, H. Chen, L. Zhang, J. Yang, Q. Shi, L.-B. Sun, J. Li, L. Li, *Chin. J. Struct. Chem.* **2024**, *10*, 100394.

[22] X. Zhang, Y. Wang, L. Yang, X. Lu, X. Suo, X. Cui, H. Xing, *Adv. Mater.* **2025**, *37*, 2501870, https://doi.org/10.1002/adma.202501870.

[23] Z. Zhang, S. B. Peh, R. Krishna, C. Kang, K. Chai, Y. Wang, D. Shi, D. Zhao, *Angew. Chem. Int. Ed.* **2021**, *60*, 17198–17204, https://doi.org/10.1002/anie.202106769.

[24] J. Cui, Z. Qiu, L. Yang, Z. Zhang, X. Cui, H. Xing, *Angew. Chem. Int. Ed.* **2022**, *61*, e202208756, https://doi.org/10.1002/anie.202208756.

[25] W. Wang, G.-D. Wang, B. Zhang, X.-Y. Li, L. Hou, Q.-Y. Yang, B. Liu, *Small* **2023**, *19*, 2302975.

[26] C. He, P. Zhang, Y. Wang, Y. Zhang, T. Hu, L. Li, J. Li, *Sep. Purif. Technol.* **2023**, *304*, 122318, https://doi.org/10.1016/j.seppur.2022.122318.

[27] Q. Liu, S. G. Cho, J. Hilliard, T.-Y. Wang, S.-C. Chien, L.-C. Lin, A. C. Co, C. R. Wade, *Angew. Chem. Int. Ed.* **2023**, *62*, e202218854, https://doi.org/10.1002/anie.202218854.

[28] Y. Xie, H. Cui, H. Wu, R.-B. Lin, W. Zhou, B. Chen, *Angew. Chem. Int. Ed.* **2021**, *60*, 9604–9609, https://doi.org/10.1002/anie.202100584.

[29] Y. Li, X. Wang, H. Zhang, L. He, J. Huang, W. Wei, Z. Yuan, Z. Xiong, H. Chen, S. Xiang, B. Chen, Z. Zhang, *Angew. Chem. Int. Ed.* **2023**, *62*, e202311419.

[30] Y. Li, L. Li, J. H. Yu, *Chem.* **2017**, *3*, 928–949.

[31] Y. Li, J. Yu, *Nat. Rev. Mater.* **2021**, *6*, 1156–1174, https://doi.org/10.1038/s41578-021-00347-3.

[32] R. B. Bai, X. W. Song, W. F. Yan, J. H. Yu, *Natl. Sci. Rev.* **2022**, *9*, nwac064.

[33] E. Pérez-Botella, S. Valencia, F. Rey, *Chem. Rev.* **2022**, *122*, 17647–17695, https://doi.org/10.1021/acs.chemrev.2c00140.

[34] D. G. Boer, J. Langerak, P. P. Pescarmona, *ACS Appl. Energy Mater.* **2023**, *6*, 2634–2656, https://doi.org/10.1021/acsaem.2c03605.

[35] M. M. Lozinska, E. Mangano, J. P. S. Mowat, A. M. Shepherd, R. F. Howe, S. P. Thompson, J. E. Parker, S. Brandani, P. A. Wright, *J. Am. Chem. Soc.* **2012**, *134*, 17628–17642, https://doi.org/10.1021/ja3070864.

[36] H. J. Choi, D. Jo, J. G. Min, S. B. Hong, *Angew. Chem. Int. Ed.* **2021**, *60*, 4307–4314, https://doi.org/10.1002/anie.202012953.

[37] X. H. Wang, N. N. Yan, M. Xie, P. Liu, P. Bai, H. Su, B. Wang, Y. Wang, L. Li, T. Cheng, P. Guo, W. Yan, J. Yu, *Chem. Sci.* **2021**, *12*, 8803–8810, https://doi.org/10.1039/D1SC00619C.

[38] V. M. Georgieva, E. L. Bruce, M. C. Verbraeken, A. R. Scott, W. J. Casteel, S. Brandani, P. A. Wright, *J. Am. Chem. Soc.* **2019**, *141*, 12744–12759, https://doi.org/10.1021/jacs.9b05539.

[39] J. Shang, G. Li, R. Singh, Q. F. Gu, K. M. Nairn, T. J. Bastow, N. Medhekar, C. M. Doherty, A. J. Hill, J. Z. Liu, P. A. Webley, *J. Am. Chem. Soc.* **2012**, *134*, 19246–19253, https://doi.org/10.1021/ja309274y.

[40] J. Shang, G. Li, R. Singh, P. Xiao, J. Z. Liu, P. A. Webley, *J. Phys. Chem. C* **2013**, *117*, 12841–12847, https://doi.org/10.1021/jp4015146.

[41] F.-X. Coudert, D. Kohen, *Chem. Mater.* **2017**, *29*, 2724–2730, https://doi.org/10.1021/acs.chemmater.6b03837.

[42] P. Cnudde, R. Demuynck, S. Vandenbrande, M. Waroquier, G. Sastre, V. V. Speybroeck, *J. Am. Chem. Soc.* **2020**, *142*, 6007–6017, https://doi.org/10.1021/jacs.9b10249.

[43] P. Cnudde, E. A. Redekop, W. Dai, N. G. Porcaro, M. Waroquier, S. Bordiga, M. Hunger, L. D. Li, U. Olsbye, V. Van Speybroeck, *Angew. Chem. Int. Ed.* **2021**, *60*, 10016–10022, https://doi.org/10.1002/anie.202017025.
[44] D. Ma, Z. Li, J. Zhu, Y. Zhou, L. Chen, X. Mai, M. Liufu, Y. Wu, Y. Li, *J. Mater. Chem. A* **2020**, *8*, 11933–11937, https://doi.org/10.1039/D0TA03151H.
[45] J. Yang, M. Tong, G. Han, M. Chang, T. Yan, Y. Ying, Q. Yang, D. Liu, *Adv. Funct. Mater.* **2023**, *33*, 2213743, https://doi.org/10.1002/adfm.202213743.
[46] C. Baerlocher, L. B. McCusker, *Database of Zeolite Structures*, IZA Structure Commission, http://www.iza-structure.org/databases/.
[47] W. Hao, X. Yan, X. Guo, W. Wang, T. Yan, J.-N. Zhang, W. Yan, *Inorg. Chem. Front.* **2023**, *10*, 1894–1906, https://doi.org/10.1039/D3QI00030C.
[48] L. Grajciar, J. Čejka, A. Zukal, C. Otero Areán, G. Turnes Palomino, P. Nachtigall, *ChemSusChem.* **2012**, *5*, 2011–2022.
[49] B. A. Reisner, Y. Lee, J. C. Hanson, G. A. Jones, J. B. Parise, D. R. Corbin, B. H. Toby, A. Freitag, J. Z. Larese, V. Kahlenberg, *Chem. Commun.* **2000**, 2221–2222, https://doi.org/10.1039/b006929i.
[50] M. M. Lozinska, J. P. S. Mowat, P. A. Wright, S. P. Thompson, J. L. Jorda, M. Palomino, S. Valencia, F. Rey, *Chem. Mater.* **2014**, *26*, 2052–2061, https://doi.org/10.1021/cm404028f.

Manuscript received: October 13, 2025
Revised manuscript received: November 18, 2025
Manuscript accepted: November 18, 2025
Version of record online: ■■, ■■